01 Mar 2022

Formulation and Processing of Dual Functional Adsorbent/ Catalyst Structured Monoliths using an Additively Manufactured Contactor for Direct Capture/Conversion of CO2 with Cogeneration of Ethylene

Shane Lawson

Khaled Baamran

Kyle Newport

Fateme Rezaei
Missouri University of Science and Technology, rezaeif@mst.edu

et. al. For a complete list of authors, see https://scholarsmine.mst.edu/che_bioeng_facwork/1054

Recommended Citation

S. Lawson et al., "Formulation and Processing of Dual Functional Adsorbent/Catalyst Structured Monoliths using an Additively Manufactured Contactor for Direct Capture/Conversion of CO2 with Cogeneration of Ethylene," *Chemical Engineering Journal*, vol. 431, article no. 133224, Elsevier, Mar 2022.
The definitive version is available at https://doi.org/10.1016/j.cej.2021.133224

Chemical Engineering Journal 431 (2022) 133224

Contents lists available at ScienceDirect

Chemical Engineering Journal

journal homepage: www.elsevier.com/locate/cej

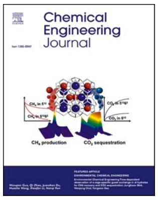

Formulation and processing of dual functional Adsorbent/Catalyst structured monoliths using an additively manufactured contactor for direct Capture/Conversion of CO_2 with cogeneration of ethylene

Shane Lawson, Khaled Baamran, Kyle Newport, Fateme Rezaei *, Ali A. Rownaghi *

Department of Chemical & Biochemical Engineering, Missouri University of Science and Technology, Rolla, MO 65409-1230, USA

ARTICLE INFO

Keywords:
Dual functional adsorbent/Catalyst Monoliths
Additive manufacturing
Combined CO_2 Capture/Conversion
Ethylene production

ABSTRACT

Utilizing CO_2 as a mild oxidant for oxidative dehydrogenation of ethane (ODHE) is an attractive way of recycling this greenhouse contaminant. Typically, CO_2 capture and conversion processes are performed in separate beds, however, combining these processes into one bed incurs advantages of lower thermal gradient and reduced energy costs. This study formulated the first generation of structured dual-functional materials (DFMs) by directly 3D printing metal-oxide-CaO/ZSM-5 inks into monolithic contactors. Specifically, we 3D-printed monoliths with V, Ga, Ni, or Ti dopants to perform metal screening and determine which metal generates the best structured DFM for combined CO_2 capture and utilization in ODHE. The samples were vigorously characterized by X-ray photoelectron spectroscopy (XPS), X-ray diffraction (XRD), N_2 physisorption, NH_3-temperature programmed desorption (NH_3-TPD), H_2-temperature programmed reduction (H_2-TPR), energy dispersive spectroscopy (EDS), and Pyridine Fourier Transform Infrared Spectroscopy (Py-FTIR). Their CO_2 capture/ODHE performances were assessed with CO_2 adsorption at 600 °C and ODHE of 25 mL/min 7% C_2H_6 at 700 °C. The combined adsorption/catalysis experiments indicated that the best performance was observed in V-CaO/ZSM-5 which achieved a staggeringly high CO_2 capture (5.4 mmol/g), 65.2% CO_2 conversion, 36.5% C_2H_6 conversion, 98% C_2H_4 selectivity, and 35.8% C_2H_4 yield as well as zero thermal cracking after 40 min-on-stream. This performance exceeded that of any previously reported material for combined CO_2 capture and ODHE utilization, indicating this novel printing method can generate DFMs with exceptional potential for combined CO_2 capture and utilization processes.

1. Introduction

Strategies towards CO_2 abatement – such as absorption, cryogenic fracturing, and adsorption – have undergone considerable advancements in the past several decades in attempts to curtail the effects of climate change stemming from this greenhouse gas [1–3]. Of the established techniques, adsorption technology – whereby CO_2 is either i) stored within a microporous material (physisorption) or ii) chemically tethered to a group-II metal oxide such as CaO (chemisorption) at high temperature – is a rapidly growing area of research because this approach can mitigate high amounts of CO_2 whilst reducing energy costs, equipment corrosion, and waste output compared to cryogenic fracturing or amine scrubbing [1,4]. Nevertheless, one criticism of all CO_2 abatement strategies, including adsorption, is that the species is usually bound to a group-II oxide to form a carbonate and buried underground for long term disposal. As might be imagined, disposing of CO_2 in this way has long been considered unattractive because this process is extremely wasteful since it continuously consumes large amounts of commodity chemicals and provides little-to-no return on investment. Hence, new strategies to effectively manage CO_2 emissions are needed.

One promising alternative to conventional CO_2 mitigation strategies is to utilize the captured emissions as a feedstock in catalytic reactions. Namely, CO_2 can be implemented as a light oxidant for paraffin dehydrogenation processes over heterogeneous bifunctional catalysts, such as oxidative dehydrogenation of ethane to ethylene. In such reactions, using CO_2 as the oxidizing source is an attractive notion because this technique allows for better control over active site reactivation compared to re-oxidation with O_2, which can lead to enhancements in light olefin selectivity, paraffin conversion, and catalyst stability by

---

* Corresponding authors.
E-mail addresses: rezaeif@mst.edu (F. Rezaei), rownaghia@mst.edu (A.A. Rownaghi).

https://doi.org/10.1016/j.cej.2021.133224
Received 24 August 2021; Received in revised form 22 October 2021; Accepted 24 October 2021
Available online 30 October 2021

shifting the equilibrium towards oxidative dehydrogenation instead of thermal cracking [5,6]. For example, we recently utilized CO_2 as a light oxidant over 3D-printed ZSM-5/metal oxide catalyst monoliths for oxidative dehydrogenation of propane to propylene and found that all samples displayed $\sim$ 10–20 enhanced propane conversions and propylene selectivity in the presence of CO_2 compared to when CO_2 was absent [7,8]. Similar findings have been reported in other works for various modes of paraffin dehydrogenation, such as ethane dehydrogenation to ethylene, so it is widely accepted that implementing CO_2 as a light oxidant is an attractive way of recycling this greenhouse contaminant [9,10]. Besides, utilizing CO_2 in this manner generally converts the species into CO, which is more marketable and can be employed in a greater variety of reactionary processes, such as metal reduction, syngas conversion to dimethyl ether, and more [11,12]. In this regard, catalytic utilization of CO_2 as a light oxidant can be considered an attractive way of managing stored CO_2 emissions from both an environmental and economic perspective.

This being the case, it is worth noting here that implementing both adsorption and catalysis steps for CO_2 capture and conversion typically requires two beds, given that most adsorption occurs at lower temperature whereas oxidative dehydrogenation of ethane (ODHE) or oxidative dehydrogenation of propane (ODHP) necessitate temperatures above 550 °C. Separating the two steps is unattractive from an industrial point-of-view because it necessitates large thermal gradients between the adsorptive and catalytic processes, leading to high energy costs. In recent years, however, researchers have sought to address this issue by performing combined adsorptive/catalytic processes in a single bed using so-called “dual-functional materials” (DFMs). Specifically, DFMs are usually comprised of high-temperature group-II metal oxide chemisorbents along with a heterogeneous catalyst (e.g., metal-doped ZSM-5) which allows for CO_2 adsorption to occur at $\sim$ 600 °C followed by a gentle thermal swing to 700 °C to desorb the CO_2 and simultaneously allow it to act as a light oxidant for oxidative dehydrogenation reactions [13,14]. Such materials were first demonstrated in our previous work where we developed DFM CaO-double salt/ZSM-5 (Cr) composites for single-bed CO_2 adsorption at 600 °C and ethane dehydrogenation at 700 °C, thus, the concept of combining adsorption and catalysis into a single bed has been proven to be viable [14].

Building upon this foundation, the next step in producing DFM materials is to form them into structured contactors (i.e., pellets, granules, or monoliths), given that powdered state adsorbent/catalysts cannot be implemented into industrial processes because of their inevitable scattering behavior, high coking tendency, and poor mass transfer properties [15,16]. Unfortunately, directly structuring double salt composites is problematic because granulation, extrusion, and pelletization processes typically require water to enable intraparticle bonding. The use of water is problematic because the adsorbent component of double salts, which contains both potassium and CaO, is highly reactive and soluble, in that the group-I metal will surely dissolve whereas exposing CaO to water will react it into $Ca(OH)_2$. Ergo, formulating structured DFMs by conventional technologies will deactivate the adsorbent and could have unforeseen consequences on the catalyst phase, as exposing ZSM-5 to $Ca(OH)_2$ could warrant some undesirable side reaction that decomposes its crystalline structure [17]. Because these issues are innate to the properties of double-salt/ZSM-5 catalysts, in that they stem from fundamental properties of the adsorbent phase, a new method is required to formulate the first generation of structured DFM adsorbent/catalyst materials.

One promising way to accomplish this goal might be to harness the power of 3D printing, otherwise known as additive manufacturing. The reason being, we recently reported a series of studies which utilized bentonite-based ceramic 3D printing to directly structure insoluble metal-oxide/ZSM-5 inks into heterogeneous catalyst monoliths [7,8,11,18,19]. Not only has this technique allowed for unprecedentedly high metal loading (35 wt% or more), but also, it can readily be applied to virtually any metal or metal-oxide and has repeatedly generated bifunctional monoliths with exceptional catalytic properties. Such properties – including reactant conversion, desired product selectivity, and prolonged stability – have been observed regardless of the reaction which has been considered. For example, our 5% Cr_2O_3-10% V_2O_5-10% Ga_2O_3-10% ZrO_2/ZSM-5 catalyst achieved a 40% propane conversion, 95% propylene selectivity, and zero deactivation after 6 h on stream for ODHP with CO_2 at 550 °C [7]. As other examples, our 4 wt% Ga_2O_3/ZSM-5 monolith achieved 85% methanol conversion and 81% dimethyl ether selectivity for methanol/dimethyl ether conversion, whereas our 15 wt% Cr_2O_3/ZSM-5 monolith achieved 80–85 % n-hexane conversion and 80% light olefin selectivity in an n-hexane cracking reaction [11,18]. Notably, these performances are amongst the highest ever reported and, given that this exceptional behavior spans across multiple reactions, it can be reasonably claimed that directly 3D-printed metal-oxide/ZSM-5 monolithic catalysts are promising materials for scale-up. As such, we sought to apply the direct printing technique to produce the first generation of DFM adsorbent/catalyst monoliths, thus providing a pathway to structure these exciting materials. However, accomplishing this task would require that some other material be substituted for CaO in the ink to prevent conversion into $Ca(OH)_2$ and reaction with ZSM-5. We theorized that the material would need to be i) insoluble in water, ii) of a sufficiently small particle size to enable bonding with bentonite clay and allow for extrusion through the printing nozzle, and iii) capable of transitioning to CaO by calcination at high temperature. To this end, we concluded that $CaCO_3$ could meet these criteria, since it is of low solubility, chemically inert, and similar in particle size to previously printed metal-oxides. Besides, $CaCO_3$ is often pyrolyzed to generate CaO anyhow, so using this material would not require extensive optimization of the activation conditions.

Motivated by this exciting possibility, we embarked on a study that performs metal screening on directly 3D-printed M−CaO/ZSM-5 monoliths in efforts of formulating the first generation of structured DFM adsorbent/catalyst materials. It should be noted here that we decided to target metal screening in this initial proof-of-concept study because our previous reports have indicated that directly 3D-printed metal-oxide/ZSM-5 monolithic catalysts display somewhat unpredictable catalytic properties, so it was difficult to spectate from present literature which dopant(s) would generate the best overall performance. It should also be noted here that we opted for combined CO_2 capture at 600 °C and ODHE conversion at 700 °C to allow for comparison to our earlier work [14]. To this end, we 3D-printed adsorbent/catalyst monoliths with 10 wt% of V, Ni, Ti, or Ga oxide catalyst dopants, 35 wt% ZSM-5 catalyst, and 43 wt% CaO adsorbent for use in a combined CO_2 adsorption and ODHE process. The monoliths were vigorously characterized by X-ray photoelectron spectroscopy (XPS), X-ray diffraction (XRD), energy dispersive spectroscopy (EDS), Pyridine Fourier Transform Infrared Spectroscopy (Py-FTIR), N_2 physisorption, NH_3-temperature programmed desorption (NH_3-TPD), and H_2-temperature programmed reduction (H_2-TPR). From the combined CO_2 adsorption and ODHE conversion process, the best performance was observed in V-CaO/ZSM-5 which achieved 65% CO_2 conversion, 36.5% C_2H_6 conversion, 98% C_2H_4 selectivity, and 36% C_2H_4 yield. Notably, this performance exceeded the best powdered sample reported previously, signifying that producing DFM adsorbent/catalysts through the direct 3D printing method is a superior pathway to formulate these materials. More importantly, this study demonstrates a simple and effective way to structure DFM adsorbent/catalyst materials, which fundamentally progresses the area of combined CO_2 capture and utilization and brings this technology one step closer to scale-up.

2. Experimental section

2.1. Materials

The following materials were purchased from Sigma Aldrich and were used for the formulation and characterization of 3D-printed adsorbent/catalyst monoliths without modification: pyridine (ACS), methylcellulose (99%), bentonite clay, $CaCO_3$ (99%), V_2O_5 (98+%), NiO (99%), TiO_2 (99%), and Ga_2O_3 (99.9%). The H-ZSM-5 (Si:Al = 30) was purchased from Zeolyst International. All UHP gases were purchased from Airgas.

2.2. Monolith formulation

The monoliths were formulated using the ink ratios shown in Table 1. The ink formulation method was identical to that which was reported in our previous works [7,8,11,18]. As before, all powder components were rolled at 60 rpm in ~ 10 mL of DI water for 48 h at ambient temperature before densifying the inks to achieve homogeneity and induce binding with bentonite. Thereafter, the inks were densified at 60 °C for ~ 4 h until a self-standing rheology was achieved whereupon they were printed to form the DFM monoliths. After printing, the monoliths were dried overnight at 25 °C in the fume hood, followed by calcination in air at 550 °C for 6 h (ramp rate = 10 °C/min) to harden the structure and convert $CaCO_3$ into CaO. Here, it should be noted that the $CaCO_3$ concentration in the pastes was greater than 50 wt%, however, calcining the $CaCO_3$ into CaO resulted in a 50:50 split of adsorbent and catalyst. It should also be noted here that performing a material balance around the metal oxide component and disregarding the weight of the CO_2 in $CaCO_3$ and the methylcellulose components can give a true approximation of the metal loadings of the catalysts which were present in the catalytic experiments. By these calculations, the metal loadings for all metal-doped samples were 10 wt%.

2.3. Characterization

The textural properties of the monoliths were evaluated with N_2 physisorption at 77 K using a Micromeritics (3Flex) gas analyzer. The surface area and pore volume were calculated by the Brunauer-Emmet-Teller (BET) and non-local density functional theory (NLDFT) methods, respectively. Prior to analysis, the monoliths were degassed at 350 °C for 6 h on a Micromeritics SmartVac prep system to remove any adsorbed species. Temperature-programmed desorption for ammonia (NH_3-TPD) and temperature-programmed reduction in hydrogen (H_2-TPR) were also performed using 3Flex to determine the active sites and redox properties of the 3D-printed monoliths. The various TPD/R methods – including the various flow rates, pretreatment conditions, thermal ramps, dwell times, and feed compositions – can be found in our previous works [20,21]. Briefly, the catalyst was first heated under 60 mL/min of He to 400 °C at 10 °C/min and held isothermally for 30 min to remove any pre-adsorbed species. Thereafter, the system was cooled to the target temperature of 80 °C. For NH_3-TPD, the sample was then saturated with 5% NH_3/He for 30 min, whereafter the bed was then purged with 40 mL/min of He for 10 min to remove any gaseous NH_3. The sample was then heated at 10 °C/min to 750 °C during which the effluent profile concentration of NH_3 was collected with a Cirrus II MKS Mass Spectrometer. The H_2-TPR procedure was similar to NH_3-TPD, except the sample bed was immediately heated at 10 °C/min to 600 °C under 5% H_2/He upon reaching the desired temperature of 80 °C, as the reduction process does not need the sample to be saturated with H_2 since the behavior measured by H_2-TPR is a reactive process and not a desorptive one. The crystalline structures of the monoliths were assessed by X-ray diffraction (XRD) on a PANalytical X'Pert multipurpose X-ray diffractometer with a scan step size of 0.02°/step at the rate of 137.2 s/step from $5 \leq 2\theta \leq 50°$. The metal dispersions were assessed using a combination of energy dispersive spectroscopy (EDS) and backscattering microscopy on a Quanta 600F ESEM with Bruker Quantax EDS. The electron orbital structures of the individual metal dopants were characterized using X-ray photoelectron spectroscopy (XPS) on a Thermoscientific Nexsa 128 channel XPS system. The scan voltage step for all metals was 0.1 eV. The scan conditions for each metal are shown in **Table S1**, **Supporting Information**. The Lewis and Brønsted acid sites were characterized using pyridine Fourier-Transform Infrared Spectroscopy (Py-FTIR) using a Nicolet iS50 FTIR equipped with an attenuated total reflectance (ATR) diamond as a supplement to NH_3-TPD. Before saturation with pyridine, the monoliths were degassed for 12 h under vacuum at 200 °C to ward off any pre-adsorbed species. The monoliths were then sealed in glass jars with beakers containing 10 mL of liquid pyridine. The sealed vessels were heated to 50 °C for 12 h to produce pyridine vapor and saturate the active sites.

2.4. CO_2 adsorption experiments

The CO_2 adsorption capacities of the monoliths were assessed on a Q500 thermalgravimetric analyzer (TGA) from TA instruments. Prior to analysis, the samples were heated at 10 °C/min under 40 mL/min of N_2 to 750 °C and were held isothermally for 1 h. The system was then cooled to 600 °C whereafter 60 mL/min of 10% CO_2/N_2 was used to saturate the monolith sample for 90 min. The CO_2 adsorption capacities of the monoliths were then calculated from the weight gain.

2.5. Catalytic assessment

The combined CO_2 capture and ODHE performances of the monoliths were assessed with an MKS Cirrus 2 Mass Spectrometer using the system detailed in our previous work [14]. Briefly, 0.2 g of sample was degassed under 40 mL/min of Ar for 1 h at 750 °C (ramp rate = 10 °C/min) prior to the experiments. The column was then cooled to 600 °C (cooling rate = 10 °C/min), whereafter 25 mL/min of 10% CO_2/Ar was flown into the column. After the sample became saturated with CO_2 (~ 1h), the column was heated at 10 °C/min to the reaction temperature of 700 °C whilst keeping under CO_2/Ar flow. Upon reaching the reaction temperature, the CO_2 feed was terminated and 25 mL/min of 7% ethane/Ar was fed into the column. The reaction was allowed to progress for 40 min. Here, it should be noted that the 3D-printed monoliths were packed into the bed with quartz wool to prevent bypass. The monoliths were ~ 1 cm in outer diameter, weight 0.2 g, and contained a cell density of 200 cells per square inch. For reference, the channel and wall geometry of the monoliths were imaged via electron microscope and are shown in **Figure S1**, **Supporting Information**.

3. Results and discussion

3.1. Characterization of 3D-Printed monoliths

The XRD spectra and metallic dispersions for the various samples are

Table 1
Ink ratios used for 3D printing DFM adsorbent/catalyst monoliths.

Sample	ZSM-5 (wt.%)	$CaCO_3$ (wt.%)	Bentonite Clay (wt.%)	Methyl-cellulose (wt.%)	V_2O_5 (wt.%)	NiO (wt.%)	TiO_2 (wt.%)	Ga_2O_3 (wt.%)
CaO/ZSM-5	29.0	59.0	10.0	2.0	0.0	0.0	0.0	0.0
V-CaO/ZSM-5	27.4	55.5	9.1	1.9	6.1	0.0	0.0	0.0
Ni-CaO/ZSM-5	27.4	55.5	9.1	1.9	0.0	6.1	0.0	0.0
Ti-CaO/ZSM-5	27.4	55.5	9.1	1.9	0.0	0.0	6.1	0.0
Ga-CaO/ZSM-5	27.4	55.5	9.1	1.9	0.0	0.0	0.0	6.1

shown in Fig. 1. Beginning with the XRD (Fig. 1**a**), it should first be noted that Ti-CaO/ZSM-5, Ni-CaO/ZSM-5, and V-CaO/ZSM-5 all displayed a strong diffractive peak at $2\theta = 29$ ° which corresponds to the [1 0 4] plane of $CaCO_3$.[22] The presence of this peak did not necessarily indicate that calcination at 550 °C failed to remove the CO_3^{2+} ion, but could have also indicated that the samples adsorbed some amount of CO_2 during cooling. This conclusion is reasonable because the calcination was performed in air, so the samples should have re-adsorbed some amount of CO_2 during the cooling step. It should also be noted that some samples did not re-adsorb CO_2 during cooling and completely lacked the [1 0 4] peak of $CaCO_3$, however, these effects seem to be random and are not suggested by any other characterizations to be dependent on the metal dopant, so the presence of the [1 0 4] plane was generally considered to be insignificant. Lastly, it should be noted that the high $CaCO_3$ concentration in some samples led to some of the diffractive peaks for ZSM-5 – e.g., those at $2\theta = 7.5°$, 8.8° – to be quite small, due to the significantly lower zeolite concentration relative to the $CaCO_3$ phase. That said, the retention of these peaks signified that the zeolite was still present and largely unaffected in the undoped, Ni-, and Ga-doped samples by the calcination processes. One could reasonably expect the majority of the crystallinity within these monoliths to be ZSM-5 when the $CaCO_3$ is calcined into CaO. More importantly, the metal-doped samples contained various diffractive indices which were consistent with the crystalline phases of the metals, signifying that the various crystalline phases were present. For example, the peak for the [1 1 1] plane of NiO was present at $2\theta = 37.5°$, whereas the [0 0 1] peak of TiO_2 was present at $2\theta = 27.5°$ and the [1 1 1] plane of Ga_2O_3 nanorods was present at $2\theta = 35°$. Granted, these peaks were not very intense which suggested low concentrations of the crystalline phases – excluding the [1 1 1] plane for Ga_2O_3 nanorods centered at $2\theta = 35°$ – so the metal-oxide phases were concluded to be mostly amorphous. Such effects were not surprising, as the commercially purchased metal-oxides were already amorphous, implying that the diffractive planes would only be present in a high concentration if the metal additives were crystallized during calcination. Obviously, this did occur to some degree, but the relatively small peak sizes of the various crystalline phases for the metal dopants indicated that the additives mostly remained amorphous. The more important data gathered from XRD was the differences in ZSM-5 diffractive indices between the various samples, as this corresponds to the degree of zeolite structural retention and somewhat correlates to the activity of the catalyst. In this regard, it should first be noted that CaO/ZSM-5, Ga-CaO/ZSM-5, Ni-CaO/ZSM-5, and V-CaO/ZSM-5 all displayed peaks at $2\theta = 7.5°$, 8.8°, 22.5°, and 49° which are consistent with the diffractive pattern for ZSM-5 powder [20]. Most of these indices were present in Ti-CaO/ZSM-5, however, that sample displayed losses in diffractive index at $2\theta = 7.5°$ and 8.8°, suggesting that titania may interact to some degree with ZSM-5 during calcination. That said, the differences in the TiO_2-doped sample regarding the ZSM-5 pattern were overall small, so it cannot be said for certain if such interactions definitively occurred, especially considering that some of the peaks may have been obscured by the $CaCO_3$ plane. On the other hand, the V-CaO/ZSM-5 sample displayed much greater degradation of the ZSM-5 structure. Notably, the losses in crystallinity for V_2O_5 were expected from our previous works because ZSM-5 is prone to dealumination by Si-OH hydration with VO_x, however, the general retention of the ZSM-5 crystalline planes for V-CaO/ZSM-5 suggested that these effects were minor compared to those which were observed in 3D-printed catalysts without the adsorbent component [7,18,23]. Nevertheless, the continued presence of the dealumination reaction seems to be a unique facet of 3D-printed VO_x/ZSM-5 catalysts formed by direct oxide printing, so subsequent works should focus on understanding why such effects occur. This is especially true when considering the Ti-CaO/ZSM-5 sample, where two diffractive indices of ZSM-5 were removed entirely, but the bulk structure of the zeolite was mostly unchanged. Such effects were reminiscent of the acidic attack from VO_x onto ZSM-5, but it is presently unclear the mechanism through which this proceeds when TiO_2 is present or why the degree of zeolite composition is less than that for V-CaO/ZSM-5. One possibility is that VO_x has more oxidative states than TiO_x, but subsequent studies which focus on understanding the differences in high-temperature behavior interactions with ZSM-5 should be performed to better understand these properties. However, such efforts should be targeted in subsequent works because this study is focused on screening metals in 3D-printed DFM monoliths for combined CO_2 capture and utilization in ODHE. In this regard, it could only be concluded from XRD that different metal dopants lead to varying degrees of ZSM-5 retention, where the highest degree of zeolite degradation was observed in V-CaO/ZSM-5 and Ti-CaO/ZSM-5.

Of course, the zeolite crystallinity is not the only structural property that pertains to catalytic activity, as dispersion of the oxide phase is also

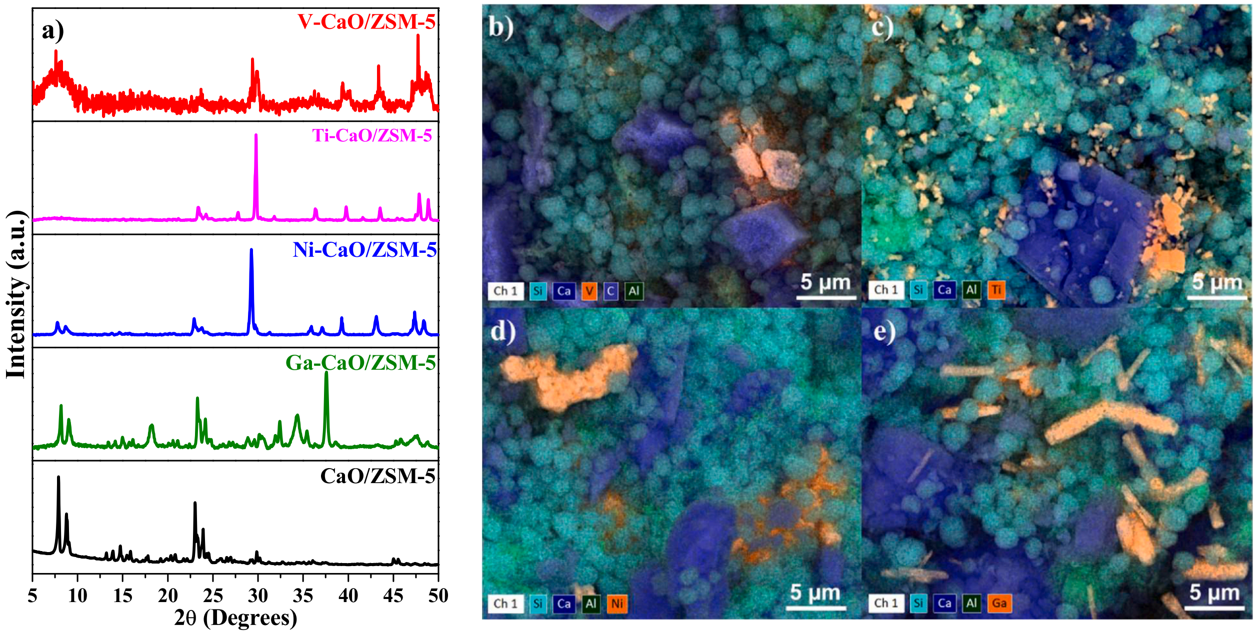

Fig. 1. (a) XRD spectra and backscatter composite EDS maps for (b) V-CaO/ZSM-5, (c) Ti-CaO/ZSM-5, (d) Ni-CaO/ZSM-5, and (e) Ga-CaO/ZSM-5.

important because an ideal catalyst is generally one which both i) retains the structure of the primary catalyst and ii) has good contact between the bifunctional components. In this regard, the EDS maps signified that the doped catalysts had varying dispersions of the metal components within the areas of assessment. From these characterizations, it should first be noted that the ZSM-5 phase – which was identified by the Si map – displayed particle sizes between 1 and 3 μm, whereas the CaO phase displayed outcropping sizes between 1 and 10 μm. Regarding the metallic dispersions, the EDS maps displayed clear differences in the metal dispersions across the samples. For example, V-CaO/ZSM-5 (Fig. 1**b**) and Ni-CaO/ZSM-5 (Fig. 1**d**) both displayed an outcropping of their metal phase, suggesting that the oxides were contained to a greater degree within the structural wall of the monolith. Meanwhile, Ti-CaO/ZSM-5 (Fig. 1**c**) and Ga-CaO/ZSM-5 (Fig. 1**e**) displayed a greater concentration of metal particles on the surface of the catalyst and appeared to have a higher degree of dispersion. Between the two, Ti-CaO/ZSM-5 appeared to have the best dispersion of the metal-oxide phase, suggesting that there may have been some synergism for that particular dopant during calcination. Granted, EDS only covers a small area of interest on the catalyst surface, so it cannot be stated for certain from the findings in Fig. 1 how the bulk metallic dispersion changes across samples. Nevertheless, Fig. 1 did indicate that i) the crystalline structure for ZSM-5 was retained to some degree in all samples and ii) the metal dopants were retained within the 3D-printed structures after calcination. As such, these results signified that the metal dopants should all impart some amount of catalytic activity for ODHE.

The XPS spectra for the metal-doped samples are shown in Fig. 2. Across all metal dopants, the expected orbital structures were observed effectively signifying that neither the ink formulation nor the calcination processes influenced the metallic oxidation states. For example, Ni-CaO/ZSM-5 (Fig. 2**a**) displayed XPS peaks at 855 eV and 872.5 eV which are consistent to the $2p_{3/2}$ and $2p_{1/2}$ orbitals, respectively, and are in good agreement with the expected spectra for Ni^{2+}.[24] Meanwhile, Ti-CaO/ZSM-5 (Fig. 2**b**) displayed peaks at 458.5 eV ($2p_{3/2}$) and 464.4 eV ($2p_{1/2}$) [25] while V-CaO/ZSM-5 (Fig. 2**c**) displayed peaks at 516 eV ($2p_{3/2}$) [26] and 525 eV ($2p_{1/2}$).[27] Finally, Ga-CaO/ZSM-5 (Fig. 2**d**) displayed a peak at 25.5 eV which corresponds to the 3d orbital of Ga^{3+}.[28] As previously mentioned, given that the electron orbitals for the various dopants agreed with the respective literature for the metals, it was concluded from Fig. 2 that the printing process did not affect the electron structure of the different metal oxides.

The N_2 physisorption isotherms and pore size distributions for the various 3D-printed monoliths are shown in Fig. 3 while the corresponding textural properties are contained in Table 2. The pore size distributions have been vertically offset to improve visual clarity. First, it should be noted that all samples displayed predominately hybridized Type I-IV physisorption behavior with Type-H_4 hysteresis (Fig. 3**a**), which is consistent with the IUPAC profiles for microporous/mesoporous materials with a hierarchal pore structure [29]. This was to be expected given that ZSM-5 is a microporous zeolite which is also slightly mesoporous. It is also worth noting that the isotherms for V-CaO/ZSM-5 and Ni-CaO/ZSM-5 showed a slightly higher slope and a larger range of pore diameters than the other three catalysts. Such behavior has been attributed to a greater amount of multilayer adsorption on the external surface of the material instead of within the internal micro/mesopores [30] and is generally indicative of some amount of pore malformation in

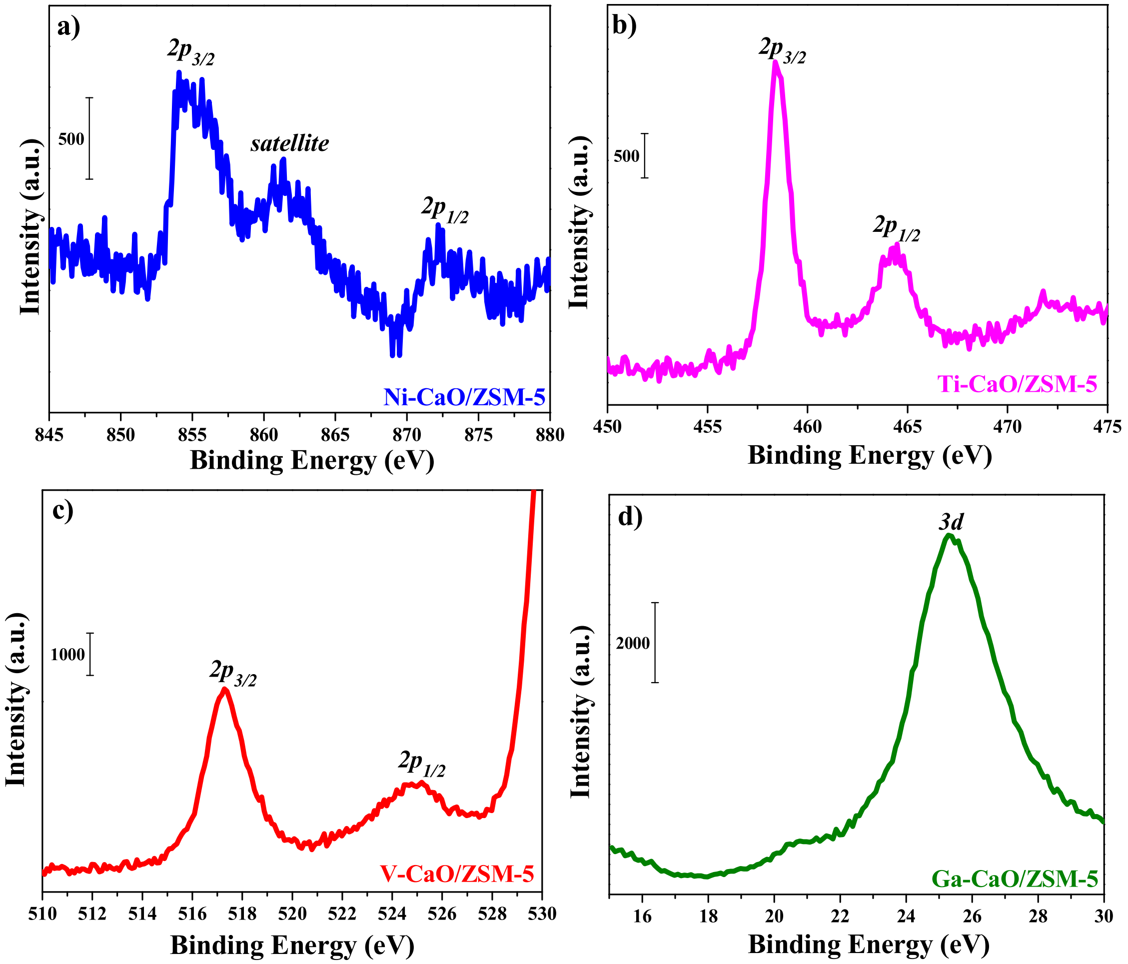

Fig. 2. XPS spectra for 3D-printed (a) Ni-CaO/ZSM-5, (b) Ti-CaO/ZSM-5, (c) V-CaO/ZSM-5, and (d) Ga-CaO/ZSM-5 adsorbent/catalyst monoliths.

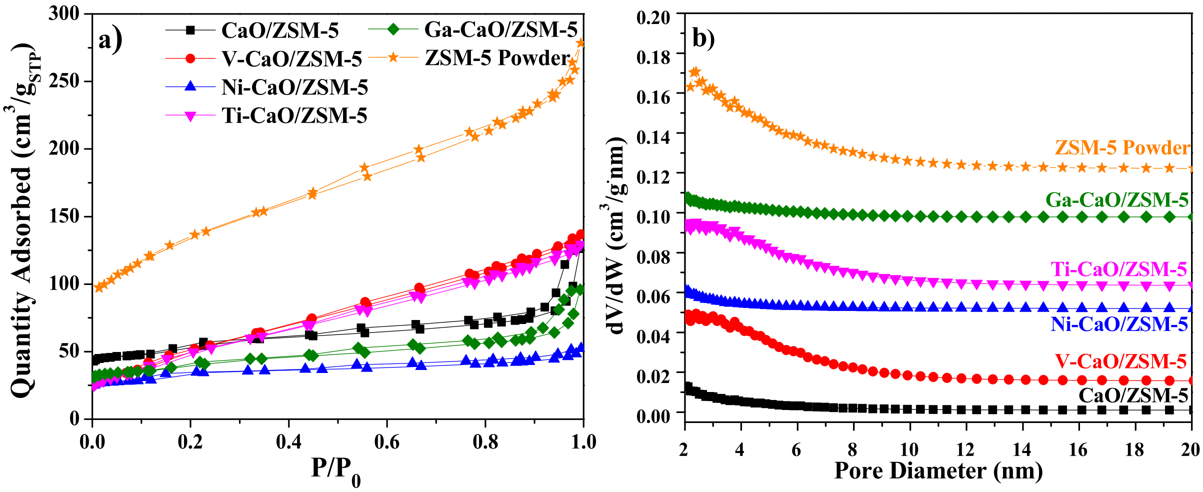

Fig. 3. (a) N_2 physisorption isotherms and (b) NLDFT pore distributions for 3D-printed DFM adsorbent catalyst monoliths.

Table 2
Textural properties of DFM catalysts from N_2 physisorption.

Sample	S_{BET} (m^2/g)	$V_{p\text{-}micro}$ (cm^3/g)	$V_{p\text{-}meso}$ (cm^3/g)	Pore Diameter (nm)
ZSM-5 Powder	470	0.16	0.22	2.5
CaO/ZSM-5	180	0.07	0.08	2.0
V-CaO/ZSM-5	210	0.03	0.07	2.0–8.0
Ni-CaO/ZSM-5	120	0.04	0.03	2.0
Ti-CaO/ZSM-5	200	0.03	0.15	2.0–8.0
Ga-CaO/ZSM-5	140	0.05	0.07	2.0

the bulk phase [31]. Harkening back to the XRD spectra in Fig. 1**a**, it was shown that the ZSM-5 structure in V-CaO/ZSM-5 and Ti-CaO/ZSM-5 was somewhat altered from the pristine CaO/ZSM-5 sample. By extension, it should therefore be expected that the textural properties of these samples were also different, since those metal dopants seemed to have some effect on the ZSM-5 structure, which is related to the pore dimensions of the zeolite. Indeed, the pore distributions (Fig. 3**b**) confirmed this theory as the V-CaO/ZSM-5 and Ti-CaO/ZSM-5 pore diameters were broader in range compared to the other samples, confirming that some changes in the pore structure were present. Further supporting these observations, the textural properties (Table 2) also suggested that the interactions between the Ti- and V-dopants with ZSM-5 generated some pore space in the ZSM-5 structure, whereas the Ga- and Ni-doped samples had lower surface areas than CaO/ZSM-5, likely stimming from pore blockage of the zeolite [11,18]. It is difficult to say for certain how these small differences will affect the performance of the monoliths for combined CO_2 adsorption and ethane dehydrogenation, however, the slight increase in textural properties for V-CaO/ZSM-5 and Ti-CaO/ZSM-5 from the other monoliths might better promote the overall adsorption rate and enhance the catalytic activity by increasing the accessibility of the active sites. Nevertheless, there are many factors which drive overall catalytic performance, so any enhancements for these samples cannot be solely allocated to the textural properties, but are likely to be caused by a combination of the metallic dispersions, catalytic acidities, textural properties, and redox behaviors. That said, Fig. 3 did signify that that all five monoliths mostly retained the expected textural properties from their ZSM-5 loading, signifying that any differences in the pore dimensions of the five catalysts were marginal, albeit with slight enhancement in textual properties for the V- and Ti-doped samples.

3.2. DFM monolith surface acidities and redox properties

The acid sites of the monoliths were analyzed by NH_3-TPD and Py-FTIR, as shown in Fig. 4. The peak areas from NH_3-TPD are contained in Table 4. Looking first at the NH_3-TPD profiles (Fig. 4**a**), it should be noted that all samples displayed a peak centered at ~ 170 °C, which corresponds to weak acid sites. A peak was also present at ~ 650 °C in all samples excluding Ga-CaO/ZSM-5, which corresponds to strong acid sites. The loss of the strong acid site peak in Ga-CaO/ZSM-5 signified that Ga_2O_3 reduced the acidity of the catalyst, which was not surprising because Ga_2O_3 is amphoteric and can act as both an acid and a base [32]. Therefore, its presence could foreseeably reduce the acid site strength. This was expected to reduce the ODHE performance of Ga-CaO/ZSM-5 because this reaction is driven by catalytic acidity, whereas basic sites tend to shift the reaction equilibrium towards thermal cracking [33,34]. Of course, such effects are not merely caused by the acid site strength but also stem from the type of acid site present. In this regard, the Py-FTIR (Fig. 4**b**) indicated that all samples contained a mixture of Lewis and Brønsted acid sites, with most of the active sites being Lewis acid sites as evidenced by the strong peak intensity at 1425 cm^{-1}. This distribution of acid sites was to be expected, given that ZSM-5 – which was the primary catalyst – can be a strong Lewis acid with slight Brønsted acidity [35]. Here, it should be noted that not all variants of ZSM-5 are dominated by Lewis acidity but this particular material contained a high Lewis acid site concentration relative to the Brønsted acid site concentration. It should finally be noted that the various metal dopants – which were present in lower concentration – imparted varying degrees of Lewis and Brønsted acidity as well but were not present in sufficiently high concentration to significantly vary the overall acidity from that of the ZSM-5 itself in a way which could be detected by Py-FTIR. Hence, the Py-FTIR only indicated that the DFM monoliths were comprised of both types of acid site but could not distinguish the ratios of said sites. However, NH_3-TPD indicated that the dopant influenced the acid site strengths and the relative concentrations of strong and weak acid sites. Therefore, culminating these characterizations indicated that the samples all contained both Lewis and Brønsted acid sites, but could be ranked in the following order based on the acid site strength and concentration which was quantified in Table 4: V-CaO/ZSM-5 ≈ Ti-CaO/ZSM-5 > Ni-CaO/ZSM-5 > Ga-CaO/ZSM-5 ≈ CaO/ZSM-5. This ranking roughly corresponds to the acidity of the catalysts, however, CaO/ZSM-5 was likely more acidic overall than Ga-CaO/ZSM-5 because the latter sample underwent a shift in acidity towards weak acid sites.

The redox properties of the various monoliths were analyzed by H_2-TPR as shown in Fig. 5. First, it should be noted here that CaO/ZSM-5 did not undergo any reduction, which is typical behavior for ZSM-5 and indicated that there was no water bonding with the alumina centers in the zeolite. In V-CaO/ZSM-5, a peak was observed at 350–400 °C, which corresponds to V_2O_5 reduction into VO_2 [36]. In Ti-CaO/ZSM-5,

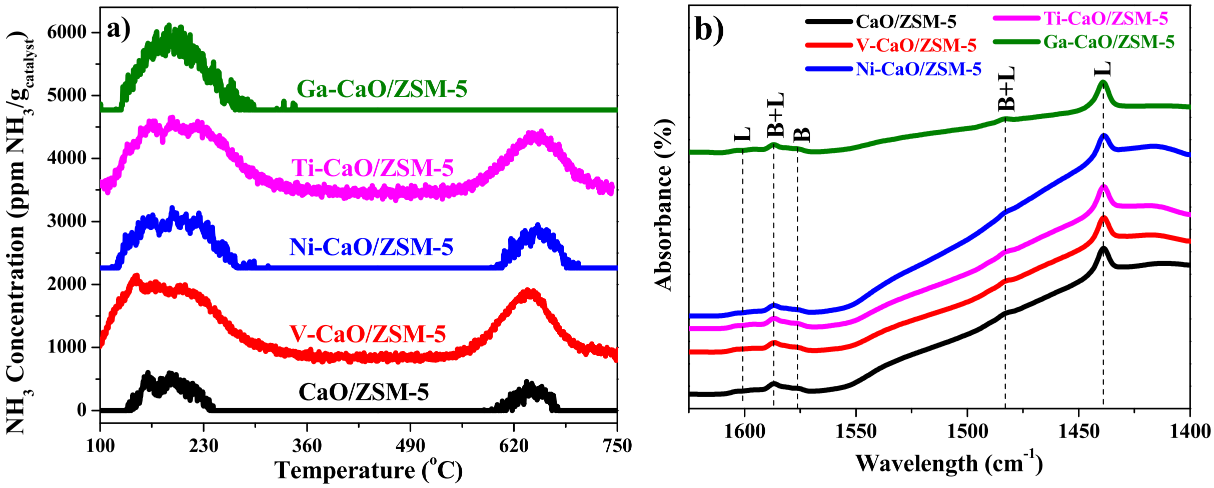

Fig. 4. (a) NH_3-TPD profiles and (b) Py-FTIR spectra of 3D-printed adsorbent/catalyst monoliths.

Table 4
Quantified NH_3 adsorbed as calculated from NH_3-TPD.

Sample	NH_3 Adsorbed (mol $NH_3/g_{catalyst}$)
CaO/ZSM-5	0.3
V-CaO/ZSM-5	1.3
Ni-CaO/ZSM-5	0.5
Ti-CaO/ZSM-5	1.3
Ga-CaO/ZSM-5	0.3

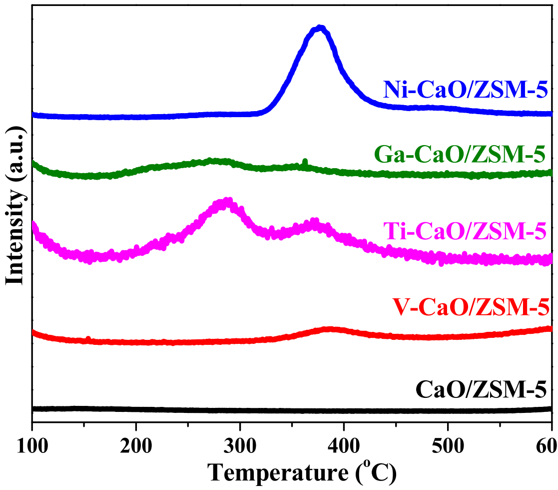

Fig. 5. H_2-TPR profiles for various DFM adsorbent/catalyst monoliths manufactured by 3D printing.

peaks were observed at 275 °C and 375 °C, which are ascribed to various modes of Ti^{2+} reduction into Ti^0. Notably, the reductions for this catalyst occurred ~ 200 °C lower than has been reported in literature [37], signifying that some synergetic effect occurred upon mixing TiO_2 with the various other components. This agreed with the high elemental dispersion for TiO_2 compared to the other samples that was observed in the EDS maps (Fig. 1), however it is difficult to say what caused this phenomenon or how it influenced the performance of Ti-CaO/ZSM-5 in combined CO_2 capture and ODHE conversion. That said, Fig. 5 did indicate that TiO_2-CaO/ZSM-5 had the greatest degree of reducibility. In Ga-CaO/ZSM-5, peaks were observed from 200 to 300 °C and 350 °C, which correspond to various modes of reduction that occur between partially substituted Ga^{3+} on ZSM-5 [38]. Notably, this partial substitution was not evidenced by either the XRD or XPS results so the degree to which it was present within the bulk of the structure was concluded to not be very high. Finally, Ni-CaO/ZSM-5 displayed a large reductive peak at 380 °C that corresponded to bulk Ni^{2+} reduction into Ni^0 [39]. Based on this dataset, the reductive potential of the catalysts could be approximated in the following order: Ti-CaO/ZSM-5 > Ni-CaO/ZSM-5 > Ga-CaO/ZSM-5 > V-CaO/ZSM-5 ⋙⋙ CaO/ZSM-5.

3.3. Combined Adsorption/Catalysis experiments

The effluent concentration profiles gathered from the adsorption/catalysis experiments as well as the CO_2 adsorption capacities collected from adsorption on TGA are displayed in Fig. 6. The corresponding reactionary results are summarized in Table 5. First looking at the CO_2 adsorption capacities of the DFM monoliths (Fig. 6**a**), the TGA analyses revealed that most of the samples adsorbed similar amounts of CO_2. However, a 15% reduction in capacity was observed for Ga-CaO/ZSM-5, suggesting that Ga_2O_3 deactivated the adsorptive sites. Literature suggests that this deactivation stemmed from Ga_2O_3 promoting the CO_2-CaO attachment in the adsorption phases, leading to a lesser degree of activation during degassing. A similar effect has been reported upon doping In_2O_3 onto double salt materials, where the valance electrons of the dopant further promote O^{2-} formation to strengthen the CO_2-CaO bonds [40]. Given that Ga_2O_3 is similar in electronic structure to In_2O_3, it is reasonable that a similar effect occurred here. Notably, this behavior only reduced the adsorption capacity in the TGA experiments where the adsorbate mixture was flown around the sample, however, it enhanced the CO_2 adsorption by a factor of three from the other monoliths in the combined adsorption/catalysis experiments (Table 5). This enhanced performance in the reaction bed likely resulted from the adsorbate flowing through the monolith channels instead of around the surface, thus providing better contact compared to TGA and a greater opportunity for Ga_2O_3 to promote CO_2 tethering to CaO. In this regard, the adsorption data indicated that, although Ga_2O_3 does reduce the total adsorption capacity of our DFM monoliths by preventing total CaO activation, it can enhance the working capacity of the material when adsorbate/adsorbent contact is sufficiently high. It should be noted here that, for all samples, the CO_2 adsorption capacity in the adsorption/reaction experiments was far less than that in TGA from Fig. 6**a**. This can be attributed to the fact that the samples were allowed to go to complete saturation in the latter set of experiments, whereas the CO_2 adsorbed in the breakthrough experiments was calculated from 5% monolith saturation per the standard method. Calculating the CO_2 adsorbed in this fashion demonstrates the differences in samples which stim from

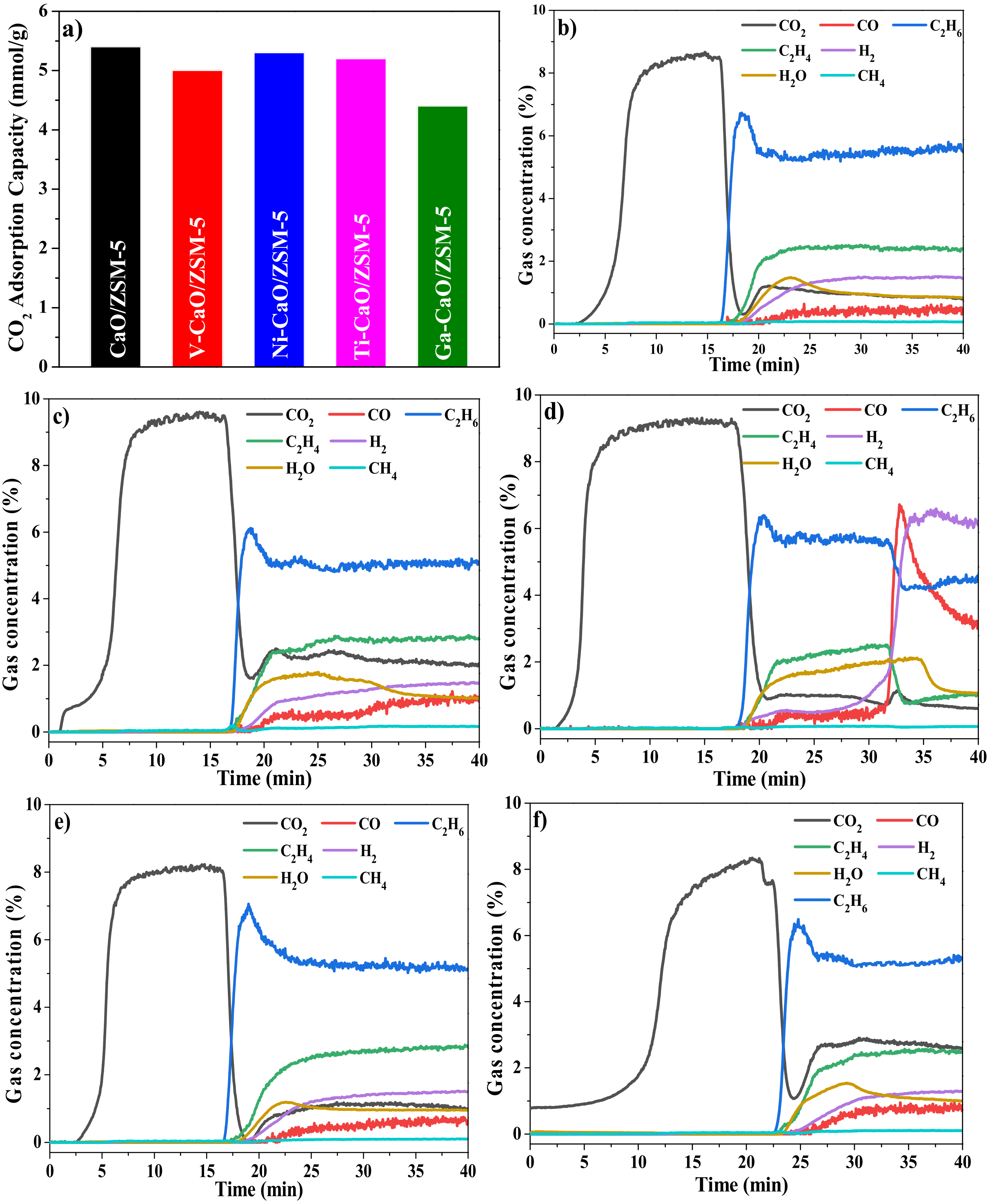

Fig. 6. (a) CO_2 adsorption capacities for different samples from TGA at 600 °C as well as effluent reaction concentration profiles for (b) CaO/ZSM-5 (c) V-CaO/ZSM-5, (d) Ni-CaO/ZSM-5, (e) Ti-CaO/ZSM-5, and (f) Ga-CaO/ZSM-5 at 700 °C under 25 mL/min of 7% C_2H_6.

variation in the monolith kinetic properties, but also leads to a lower working adsorption capacity compared to that which is observed at full saturation by CO_2, as is the case in TGA. However, the adsorption capacity calculated from breakthrough is generally considered to be a better metric with regards to understanding the working performances of the catalysts [19].

Moving onto the reactionary data, such differences in kinetic behavior lead to variation in the degree of CO_2 utilization across samples. In particular, the strong binding in Ga-CaO/ZSM-5 (Fig. 6**f**), led to a lesser degree of utilization due to a greater bond strength in $CaCO_3$ by way of the Ga_2O_3 promotional effect. Nevertheless, the Ga-CaO/ZSM-5 still outperformed the undoped CaO/ZSM-5 monolith (Fig. 6**b**) regarding overall ethylene yield, so there was some benefit imparted by doping the catalyst with Ga_2O_3. In fact, the performance of Ga-CaO/ZSM-5 lied in the middle of the various catalysts, as the combined adsorption/catalysis experiments indicated that the ethylene yield for

Table 5
Summary of results from combined CO_2 adsorption/ethane dehydrogenation experiments over 3D-printed DFM catalyst monoliths.

Sample	CO_2 Adsorbed (mmol/g)	CO_2 Conversion (%)	C_2H_6 Conversion (%)	C_2H_4 Selectivity (%)	C_2H_4 Yield (%)
CaO/ZSM-5	1.3	27.1	34.3	79.8	27.4
V-CaO/ZSM-5	1.3	65.2	36.5	98.0	35.8
Ni-CaO/ZSM-5	1.0	66.0	28.9	96.8	28.0
Ti-CaO/ZSM-5	1.1	29.7	33.9	97.5	33.1
Ga-CaO/ZSM-5	3.3	11.2	33.7	91.3	30.7

the different samples could be ranked in the following order: V-CaO/ZSM-5 > Ti-CaO/ZSM-5 > Ga-CaO/ZSM-5 > Ni-CaO/ZSM-5 > CaO/ZSM-5. Notably, this ranking did not perfectly align with the catalytic acidities which were determined from Fig. 4, but the most acidic sample – i.e., V-CaO/ZSM-5 – did display the best performance. The high performance of V-CaO/ZSM-5 suggests that the catalyst acidity is certainly an important factor to the performance of 3D-printed DFM materials, but the differences in this ranking compared to the ranking of acidity also suggest that other factors – such as the redox properties or CO_2/CaO bond strength – play a significant role in the catalytic behavior.

Between V-CaO/ZSM-5 (Fig. 6**c**) and Ti-CaO/ZSM-5 (Fig. 6**e**), the former sample displayed exceptional CO_2 conversion whereas the latter sample did not effectively utilize CO_2. This behavior likely signified that the VO_x clusters were continuously re-oxidized by the desorbing CO_2, whereas TiO_2 displayed catalytic behavior that was more consistent with thermal cracking instead of oxidative dehydrogenation. To be more specific, the high CO_2 conversion for V-CaO/ZSM-5 was likely caused by the high acidity of vanadium as well as the numerous oxidation states of VO_x, which allow this particular metal to rapidly switch between electron donation and acceptance, thus promoting strong interactions with CO_2 [5,41]. Notably, Ni-CaO/ZSM-5 (Fig. 6**d**) achieved a similar CO_2 conversion to that of V-CaO/ZSM-5, however, that sample underwent a shift in reaction equilibrium to thermal cracking at $t = 30$ min while V-CaO/ZSM-5 continued reacting with C_2H_6 via oxidative dehydrogenation. In turn, Ni-CaO/ZSM-5 displayed overall worse performance than V-CaO/ZSM-5. Granted, the high conversion of CO_2 for Ni-CaO/ZSM-5 suggested that this sample is especially promising for CO_2 utilization, so there could be some benefit for lightly doping DFM adsorbent/catalysts with small amounts of NiO. However, co-doping these materials should be targeted in subsequent works because this study is focused on initial metal screening for 3D-printed DFM adsorbent/catalyst monoliths in combined CO_2 capture and ODHE conversion. In this regard, Fig. 6 and Table 5 indicated that directly 3D printing DFM adsorbent/catalyst monoliths can generate materials with outstanding performance. In fact, all samples achieved ethylene yields that were at least comparable to the double salt/ZSM-5 powders reported previously [14], where V-CaO/ZSM-5 increased the ethylene yield from 22% to 35.8% and the CO_2 conversion from 14% to 65.2%. As far as are aware, this is the best performance ever reported for this combined process. Even compared to heterogeneous catalysts for ODHE reaction without the adsorption step, such as Cr-TUD-1 (23–37.5% C_2H_6 conversion) [42], Cr/ZSM-5 (37% C_2H_4 yield) [43], or VOx/Al_2O_3-ZrO_2 composites (8.5% C_2H_6 conversion and 82% C_2H_4 selectivity) [44], these DFM materials displayed ODHE performances that were well within an acceptable range. Granted, the various parameters of space velocity, reaction temperature, bed orientation, monolith geometry, and long-term stability still need to be investigated for these catalysts, but the first step in optimizing such properties is to determine the materials which should be used. In this regard, this study firmly cements that 3D-printed V-CaO/ZSM-5 DFM monoliths are exceptional materials for combined CO_2 capture and ODHE utilization. More importantly, this work establishes the first generation of structured DFM adsorbent/catalyst monoliths for combined CO_2 capture and ODHE conversion and demonstrates that the direct metal-oxide 3D printing technique as a remarkable pathway through which to structure heterogeneous catalyst materials.

4. Conclusions

In this work we formulated the first-generation of DFM adsorbent/catalyst monoliths for use in combined CO_2 capture and utilization in a ODHE process by directly printing M−$CaCO_3$/ZSM-5 inks. Specifically, we performed metal screening to determine which dopant (V, Ga, Ni, or Ti) produced the best overall CO_2 adsorption/ODHE conversion performance. The samples were characterized by a myriad of techniques which revealed that the metal dopants did not significantly change the structure of the bulk ZSM-5, however, Ga_2O_3 doping was found to reduce the acidity of the DFM composites from the other dopants. More importantly, the combined adsorption/catalysis experiments indicated that all samples displayed improved performance compared to double salt/ZSM-5 materials, where V-CaO/ZSM-5 achieved a staggeringly high 65.2% CO_2 conversion, 36.5% C_2H_6 conversion, 98% C_2H_4 selectivity, and 35.8% C_2H_4 yield. To the best of our knowledge, this performance is the best which has ever been reported for single-bed CO_2 adsorption/ODHE conversion and represents a fundamental breakthrough in material formulation for DFM composites. Besides, this study reports the first-generation of structured DFM adsorbent/catalysis monoliths, which demonstrates a simple and effective pathway through which to form DFMs into practical monolithic contactors. Not to be overlooked, this advancement is important in and of itself because, before this study, there was no known way to structure DFMs into practical geometric contactors, thus their usability in industrial processes was limited until now. As such, this work furthers the areas of both CO_2 capture and conversion as well as DFM material formulation, since it demonstrates a novel pathway through which to structure DFMs and provides a composite material that displays exceptional performance in combined CO_2 capture/ODHE conversion.

Declaration of Competing Interest

The authors declare that they have no known competing financial interests or personal relationships that could have appeared to influence the work reported in this paper.

Acknowledgements

The authors acknowledge the electron microscopy core (EMC) at University of Missouri Columbia for taking the backscatter images and elemental maps. The authors also acknowledge the materials research center (MRC) at Missouri University of Science and Technology for performing the XRD and XPS characterizations. The involvement of S.L. in this work was sponsored by the National Science Foundation internship program (NSF CBET-1802049).

Appendix A. Supplementary data

Supplementary data to this article can be found online at https://doi.org/10.1016/j.cej.2021.133224.

References

[1] T. Gelles, S. Lawson, A.A. Rownaghi, F. Rezaei, Recent advances in development of amine functionalized adsorbents for CO2 capture, Adsorption 26 (1) (2020) 5–50, https://doi.org/10.1007/s10450-019-00151-0.

[2] C.A. Grande, R. Blom, Utilization of dual - PSA technology for natural gas upgrading and integrated CO2 capture, Energy Procedia 26 (2012) 2–14, https://doi.org/10.1016/j.egypro.2012.06.004.

[3] A. Al-Mamoori, A. Krishnamurthy, A.A. Rownaghi, F. Rezaei, Carbon capture and utilization update, Energy Technol. 5 (6) (2017) 834–849, https://doi.org/10.1002/ente.201600747.

[4] A. Samanta, A. Zhao, G.K.H. Shimizu, P. Sarkar, R. Gupta, Post-combustion CO2 capture using solid sorbents: a review, Ind. Eng. Chem. Res. 51 (4) (2012) 1438–1463.

[5] M.A. Atanga, F. Rezaei, A. Jawad, M. Fitch, A.A. Rownaghi, Oxidative dehydrogenation of propane to propylene with carbon dioxide, Appl. Catal. B Environ. 220 (2018) 429–445, https://doi.org/10.1016/j.apcatb.2017.08.052.

[6] M.B. Ansari, S.E. Park, Carbon dioxide utilization as a soft oxidant and promoter in catalysis, Energy Environ. Sci. 5 (2012) 9419–9437, https://doi.org/10.1039/c2ee22409g.

[7] S. Lawson, A. Farsad, B. Adebayo, K. Newport, K. Schueddig, E. Lowrey, F. Polo-Garzon, F. Rezaei, A.A. Rownaghi, A novel method of 3D printing high-loaded oxide/H-ZSM-5 catalyst monoliths for carbon dioxide reduction in tandem with propane dehydrogenation, Adv. Sustain. Syst. 5 (3) (2021), https://doi.org/10.1002/adsu.202000257.

[8] S. Lawson, K.A. Newport, A. Axtell, C. Boucher, B. Grant, M. Haas, M. Lee, F. Rezaei, A.A. Rownaghi, Structured bifunctional catalysts for CO2 activation and oxidative dehydrogenation of propane, ACS Sustain. Chem. Eng. 9 (16) (2021) 5716–5727, https://doi.org/10.1021/acssuschemeng.1c00882.

[9] E. Nowicka, C. Reece, S.M. Althahban, K.M.H. Mohammed, S.A. Kondrat, D. J. Morgan, Q. He, D.J. Willock, S. Golunski, C.J. Kiely, G.J. Hutchings, Elucidating the role of CO2 in the soft oxidative dehydrogenation of propane over ceria-based catalysts, ACS Catal. 8 (4) (2018) 3454–3468, https://doi.org/10.1021/acscatal.7b03805.

[10] S. Yao, B. Yan, Z. Jiang, Z. Liu, Q. Wu, J.H. Lee, J.G. Chen, Combining CO2 reduction with ethane oxidative dehydrogenation by oxygen-modification of molybdenum carbide, ACS Catal. 8 (6) (2018) 5374–5381, https://doi.org/10.1021/acscatal.8b00541.

[11] F. Magzoub, S. Lawson, F. Rezaei, A.A. Rownaghi, Directly printed oxide/ZSM-5 bifunctional catalysts for methanol conversion to dimethyl ether with exceptional stability, conversion, and selectivity, Energy Fuels 35 (3) (2021) 2619–2629, https://doi.org/10.1021/acs.energyfuels.0c04279.

[12] L. Wang, S.A. Nitopi, E. Bertheussen, M. Orazov, C.G. Morales-Guio, X. Liu, D. C. Higgins, K. Chan, J.K. Nørskov, C. Hahn, T.F. Jaramillo, Electrochemical Carbon monoxide reduction on polycrystalline copper: effects of potential, pressure, and pH on selectivity toward multicarbon and oxygenated products, ACS Catal. 8 (8) (2018) 7445–7454, https://doi.org/10.1021/acscatal.8b01200.

[13] A. Al-Mamoori, H. Thakkar, X. Li, A.A. Rownaghi, F. Rezaei, Development of potassium- and sodium-promoted CaO adsorbents for CO2 capture at high temperatures, Ind. Eng. Chem. Res. 56 (29) (2017) 8292–8300, https://doi.org/10.1021/acs.iecr.7b01587.

[14] A. Al-Mamoori, S. Lawson, A.A. Rownaghi, F. Rezaei, Oxidative dehydrogenation of ethane to ethylene in an integrated CO2 capture-utilization process, Appl. Catal. B Environ. 278 (2020) 119329, https://doi.org/10.1016/j.apcatb.2020.119329.

[15] M.S. Duyar, M.A.A. Treviño, R.J. Farrauto, Dual function materials for CO2 capture and conversion using renewable H2, Appl. Catal. B: Environ. 168–169 (2015) 370–376.

[16] C. Jeong-Potter, R. Farrauto, Feasibility study of combining direct air capture of CO2 and methanation at isothermal conditions with dual function materials, Appl. Catal. B: Environ. 282 (2021), 119416.

[17] J. Yan, C.Y. Zhao, Experimental study of CaO/Ca(OH)2 in a fixed-bed reactor for thermochemical heat storage, Appl. Energy 175 (2016) 277–284, https://doi.org/10.1016/j.apenergy.2016.05.038.

[18] S. Lawson, A. Farsad, F. Rezaei, D. Ludlow, A.A. Rownaghi, Direct ink writing of metal oxide/H-ZSM-5 catalysts for n-hexane cracking: a new method of additive manufacturing with high metal oxide loading, ACS Appl. Mater. Interfaces 13 (1) (2021) 781–794, https://doi.org/10.1021/acsami.0c20752.

[19] S. Lawson, X. Li, H. Thakkar, A.A. Rownaghi, F. Rezaei, Recent advances in 3D printing of structured materials for adsorption and catalysis applications, Chem. Rev. 121 (10) (2021) 6246–6291, https://doi.org/10.1021/acs.chemrev.1c00060.

[20] X. Li, F. Rezaei, A. Rownaghi, Methanol-to-olefin conversion on 3D-printed ZSM-5 monolith catalysts: Effects of metal doping, mesoporosity and acid strength, Microporous Mesoporous Mater. 276 (2019) 1–12, https://doi.org/10.1016/j.micromeso.2018.09.016.

[21] F. Magzoub, X. Li, J. Al-darwish, F. Rezaei, A.A. Rownaghi, 3D-printed ZSM-5 monoliths with metal dopants for methanol conversion in the presence and absence of carbon dioxide, Appl. Catal. B Environ. 245 (2019) 486–495, https://doi.org/10.1016/j.apcatb.2019.01.008.

[22] Q. Shen, H. Wei, L. Wang, Y. Zhou, Y. Zhao, Z. Zhang, D. Wang, G. Xu, D. Xu, Crystallization and aggregation behaviors of calcium carbonate in the presence of poly (vinylpyrrolidone) and sodium dodecyl sulfate, J. Phys. Chem. B. 109 (39) (2005) 18342–18347.

[23] M. Petras, B. Wichterlova, High-temperature interaction of vanadium pentoxide with H-ZSM-5 zeolite. ESR and IR study, J. Phys. Chem. 96 (4) (1992) 1805–1809, https://doi.org/10.1021/j100183a056.

[24] W. Yang, X. Yang, J. Jia, C. Hou, H. Gao, Y. Mao, C. Wang, J. Lin, X. Luo, Oxygen vacancies confined in ultrathin nickel oxide nanosheets for enhanced electrocatalytic methanol oxidation, Appl. Catal. B Environ. 244 (2019) 1096–1102, https://doi.org/10.1016/j.apcatb.2018.12.038.

[25] W. Ren, Z. Ai, F. Jia, L. Zhang, X. Fan, Z. Zou, Low temperature preparation and visible light photocatalytic activity of mesoporous carbon-doped crystalline TiO2, Appl. Catal. B Environ. 69 (3-4) (2007) 138–144, https://doi.org/10.1016/j.apcatb.2006.06.015.

[26] D.P. Debecker, K. Bouchmella, R. Delaigle, P. Eloy, C. Poleunis, P. Bertrand, E. M. Gaigneaux, P.H. Mutin, One-step non-hydrolytic sol – gel preparation of efficient V2O5 -TiO2 catalysts for VOC total oxidation, Appl. Catal. B Environ. 94 (1-2) (2010) 38–45, https://doi.org/10.1016/j.apcatb.2009.10.018.

[27] G. Silversmit, D. Depla, H. Poelman, G.B. Marin, R. De Gryse, An XPS study on the surface reduction of V2O5 (001) induced by Ar+ ion bombardment, Surf. Sci. 600 (17) (2006) 3512–3517, https://doi.org/10.1016/j.susc.2006.07.006.

[28] B.R. Tak, S. Dewan, A. Goyal, R. Pathak, V. Gupta, A.K. Kapoor, S. Nagarajan, R. Singh, Point defects induced work function modulation of β-Ga2O3, Appl. Surf. Sci. 465 (2019) 973–978, https://doi.org/10.1016/j.apsusc.2018.09.236.

[29] M. Thommes, K. Kaneko, A.V. Neimark, J.P. Olivier, F. Rodriguez-Reinoso, J. Rouquerol, K.S.W. Sing, Physisorption of gases, with special reference to the evaluation of surface area and pore size distribution (IUPAC Technical Report), Pure Appl. Chem. 87 (2015). https://doi.org/10.1515/pac-2014-1117.

[30] K.S.W. Sing, Physisorption of nitrogen by porous materials, J. Porous Mater. 2 (1) (1995) 5–8, https://doi.org/10.1007/BF00486564.

[31] S. Storck, H. Bretinger, W.F. Maier, Characterization of micro- and mesoporous solids by physisorption methods and pore-size analysis, Appl. Catal. A Gen. 174 (1-2) (1998) 137–146.

[32] P.B. Sanguineti, M.A. Baltanás, A.L. Bonivardi, Copper-gallia interaction in Cu-Ga2O3-ZrO2 catalysts for methanol production from carbon oxide(s) hydrogenation, Appl. Catal. A Gen. 504 (2015) 476–481, https://doi.org/10.1016/j.apcata.2014.11.021.

[33] Z. Shen, J. Liu, H. Xu, Y. Yue, W. Hua, W. Shen, Applied catalysis A: General Dehydrogenation of ethane to ethylene over a highly efficient Ga2O3/HZSM-5 catalyst in the presence of CO2, Appl. Catal. A Gen. 356 (2) (2009) 148–153, https://doi.org/10.1016/j.apcata.2008.12.038.

[34] A.N. Matveyeva, J. Wärnå, N.A. Pakhomov, D. Yu. Murzin, Kinetic modeling of isobutane dehydrogenation over Ga2O3/Al2O3 catalyst, Chem. Eng. J. 381 (2020) 122741, https://doi.org/10.1016/j.cej.2019.122741.

[35] V. Boosa, S. Varimalla, M. Dumpalapally, N. Gutta, V.K. Velisoju, N. Nama, V. Akula, Influence of Brønsted acid sites on chemoselective synthesis of pyrrolidones over H-ZSM-5 supported copper catalyst, Appl. Catal. B Environ. 292 (2021) 120177, https://doi.org/10.1016/j.apcatb.2021.120177.

[36] S.M. Jung, P. Grange, Characterization and reactivity of V2O5 -WO3 supported on TiO2-SO42 − catalyst for the SCR reaction, Appl. Catal. B Environ. 32 (1-2) (2001) 123–131.

[37] M. Xu, S. He, H. Chen, G. Cui, L. Zheng, B. Wang, M. Wei, TiO 2–x -Modified Ni Nanocatalyst with Tunable Metal − Support Interaction for Water − Gas Shift Reaction, ACS Catal. 7 (11) (2017) 7600–7609, https://doi.org/10.1021/acscatal.7b01951.

[38] T.A. Zepeda, B. Pawelec, A. Infantes-Molina, R.I. Yocupicio, G. Alonso-Núñez, S. Fuentes, J.N. Diaz de León, J.L.G. Fierro, Ortho-xylene hydroisomerization under pressure on HMS-Ti mesoporous silica decorated with Ga2O3 nanoparticles, Fuel 158 (2015) 405–415, https://doi.org/10.1016/j.fuel.2015.05.056.

[39] H. Mori, C. Wen, J. Otomo, K. Eguchi, H. Takahashi, Investigation of the interaction between NiO and yttria-stabilized zirconia (YSZ) in the NiO/YSZ composite by temperature-programmed reduction technique, Appl. Catal. A Gen. 245 (2003) 79–85, https://doi.org/10.1016/S0926-860X(02)00634-8.

[40] T. Alghamdi, K.S. Baamran, M.U. Okoronkwo, A.A. Rownaghi, F. Rezaei, Metal-Doped K − Ca double salts with improved capture performance and stability for high-temperature CO2 adsorption, Energy Fuels 35 (5) (2021) 4258–4266, https://doi.org/10.1021/acs.energyfuels.0c04385.

[41] Y.u. Gu, H. Liu, M. Yang, Z. Ma, L. Zhao, W. Xing, P. Wu, X. Liu, S. Mintova, P. Bai, Z. Yan, Highly stable phosphine modified VOx/Al2O3 catalyst in propane dehydrogenation, Appl. Catal. B Environ. 274 (2020) 119089, https://doi.org/10.1016/j.apcatb.2020.119089.

[42] M. Numan, T. Kim, C. Jo, S.-E. Park, Ethane Dehydrogenation with CO2as a soft oxidant over a Cr-TUD-1 catalyst, J. CO2 Util. 39 (2020) 101184, https://doi.org/10.1016/j.jcou.2020.101184.

[43] N. Mimura, M. Okamoto, H. Yamashita, S.T. Oyama, K. Murata, Oxidative dehydrogenation of ethane over Cr/ZSM-5 catalysts using CO2 as an oxidant, J. Phys. Chem. B. 110 (43) (2006) 21764–21770, https://doi.org/10.1021/jp061966l.

[44] M.H. Jeong, J. Sun, G. Young Han, D.H. Lee, J.W. Bae, Successive reduction-oxidation activity of FeOx/TiO2 for dehydrogenation of ethane and subsequent CO2 activation, Appl. Catal. B Environ. 270 (2020) 118887, https://doi.org/10.1016/j.apcatb.2020.118887.